energies

MDPI

Article

A Laser-Based Heating System for Studying the Morphological Stability of Porous Ceria and Porous $La_{0.6}Sr_{0.4}MnO_3$ Perovskite during Solar Thermochemical Redox Cycling

Kangjae Lee and Jonathan R. Scheffe *

Department of Mechanical and Aerospace Engineering, University of Florida, Gainesville, FL 32611, USA; anakin27@ufl.edu

* Correspondence: jscheffe@ufl.edu

Received: 10 October 2020; Accepted: 6 November 2020; Published: 13 November 2020



Abstract: Thermochemical processes are considered promising pathways to utilize solar energy for fuel production. Several physico-chemical, kinetic and thermodynamic properties of candidate oxides have been studied, yet their morphological stability during redox cycling under radiative heating is not widely reported. Typically when it is reported, it is for large-scale directly irradiated reactors (~1–10 kW_{th}) aimed at demonstrating high efficiency, or in indirectly irradiated receivers where the sample surface is not exposed directly to extreme radiative fluxes. In this work, we aimed to emulate heat flux conditions expected in larger scale solar simulators, but at a smaller scale where experimentation can be performed relatively rapidly and with ease compared to larger prototype reactors. To do so, we utilized a unique infrared (IR) laser-based heating system with a peak heat flux of 2300 kW/m^2 to drive redox cycles of two candidate materials, namely nonstoichiometric $CeO_{2-\delta}$ and $La_{0.6}Sr_{0.4}MnO_{3-\delta}$. In total, 200 temperature-swing cycles using a porous ceria pellet were performed at constant pO_2, and 5 cycles were performed for both samples by introducing H_2O vapor into the system during reduction. Porous ceria pellets with porosity (0.55) and pore size (4–7 μm) were utilized because of their similarity to other porous structures utilized in larger-scale reactors. Overall, we observed that reaction extents initially decreased along with the decrease in reaction rates up to cycle 120 because of the change in structure and sintering. In the case of H_2O splitting, ceria outperformed LSM40 in total H_2 production because of the low pO_2 during oxidation, where the oxidation of LSM40 is less favorable than that of ceria.

Keywords: laser heating; morphological stability; porous; ceria; perovskite; solar; thermochemical; fuel

1. Introduction

Thermochemical processes are one of several promising pathways capable of utilizing solar energy to produce hydrocarbon fuel precursors or pure H_2 via the splitting of CO_2 and/or H_2O [1–4]. These operate via two-step reduction and oxidation (redox) cycles using metal oxides as a reactive intermediate. Ceria ($CeO_{2-\delta}$) is considered the state-of-the-art metal oxide [5,6] and the chemical reactions enabling this process using ceria are shown below [7–9].

$$\text{Reduction: } CeO_{2-\delta i} \rightarrow CeO_{2-\delta f} + 0.5(\delta_f - \delta_i)\, O_2\ (g)$$

$$H_2O \text{ Splitting: } CeO_{2-\delta f} + (\delta_f - \delta_i)\, H_2O\ (g) \rightarrow CeO_{2-\delta i} + (\delta_f - \delta_i)\, H_2\ (g)$$

$$CO_2 \text{ Splitting: } CeO_{2-\delta f} + (\delta_f - \delta_i)\, CO_2\ (g) \rightarrow CeO_{2-\delta i} + (\delta_f - \delta_i)\, CO\ (g)$$

The first reaction is an endothermic reduction at elevated temperature (e.g., $T > 1200$ °C) enabled using solar thermal energy, and the second lower temperature (e.g., $T < 1000$ °C) and exothermic reaction, shown here using either H_2O or CO_2, re-oxidizes ceria to produce either H_2 or CO. δ_i and δ_f refer to the initial and final oxygen non-stoichiometry of ceria, respectively, and are functions of temperature and pO_2. Reduction is typically initiated at partial pressures of oxygen in the range ($10^{-2} > pO_2 > 10^{-7}$ atm) and is accompanied by the release in oxygen corresponding to $0.5(\delta_f - \delta_i)$ mol per mol of ceria.

In general, ceria has favorable thermal and physical properties for redox processes. For example, it is physically stable at high temperatures (i.e., withstands sintering) [6,10], oxidation is thermodynamically favorable over a wide range of oxidation conditions (which limits the required temperature-swing and sensible heating of the solid) [6], and reaction kinetics of both steps are rapid due to high oxygen diffusivities in the bulk and rapid surface exchange [5,6,11,12]. Marxer et al. recently achieved a solar-to-fuel efficiency of 5.25% using an engineered reticulated porous ceramic (RPC) of ceria contained within a cavity-based receiver [8]. It contains large pores (i.e., 2.5 mm mean diameter) for enhanced radiative heat transfer and small pores (i.e., 10 μm mean diameter) for enhanced reaction rates. In addition to ceria, perovskites with ABO_3 structure have gained interest because of the potential A-site and B-site dopant combinations that can achieve higher reduction extents (δ_{red}) and at lower temperatures compared to that of ceria. In effect, they have the potential to be "tuned" to alter their thermodynamic and kinetic properties to those that are more desirable. Several of the perovskites investigated are from the La-Sr-Mn class of perovskites, for example $La_{0.6}Sr_{0.4}MnO_3$ (LSM40) [13], $La_{0.7}Sr_{0.3}MnO_3$ (LSM30) [13,14], and $La_{0.4}Sr_{0.6}Mn_{0.6}Al_{0.4}O_3$ (LSMA4664) [15–17].

For any candidate redox material it is crucial for the oxide to be morphologically stable at high temperatures (e.g., $T > 1400$ °C) especially in the case of directly irradiated reactors/receivers like Marxer et al., where the surface can be much hotter than the bulk [8]. The long-term morphological stability of ceria has been studied in the literature by various groups in several different ways. Chueh et al. prepared porous monoliths of ceria and 15 mol% Sm-doped ceria with 65% porosity and heated the samples indirectly in an alumina tube that was placed inside an infrared heated furnace for 500 consecutive cycles [1]. The samples were cycled between 1500 °C ($pO_2 = 10^{-5}$ atm, 10 min) and 800 °C ($pH_2O = 0.13$ to 0.15 atm, 10 min), and the oxidation and reduction reaction rates became essentially constant for 400 cycles after an initial stabilization period of 100 cycles where they decreased due to sintering. Gladen et al. also utilized an alumina tube placed in an infrared furnace to cycle fibrous ceria particles for 1000 isothermal cycles followed by 16 temperature-swing cycles [18]. The samples were cycled isothermally at 1500 °C with N_2 (99.998% with $O_2 < 10$ ppm) during reduction and CO_2 (99.999%) during oxidation. For temperature-swing cycling, the samples were cycled between 1500 °C with N_2 800 °C with 25 mol% CO_2. Even with the decrease in specific surface area to 56% of the initial specific surface area, fibrous ceria retained a porous microstructure and 89% of the peak fuel production with a stable average production rate after 300 cycles. Hathaway et al. demonstrated 45 isothermal redox cycles in an indirectly radiated reactor operated at 1477 °C [19]. Ceria powder within the alumina tube was reduced in a N_2 environment and oxidized with CO_2; the CO production was stable throughout the 45 cycles with an average of 360 mL/min. Marxer et al. performed 500 cycles in a directly radiated cavity reactor (4 kW) operating between 1500 °C in an Ar environment and 600 °C using H_2O followed by further oxidation with air at 600 °C [8]. The dual-scale porous RPC structure enhanced both reduction and oxidation rates by enhancing the heat and mass transport properties, and the μm-sized pores within the RPC struts were preserved after 500 cycles. Specific O_2 yield was almost constant throughout 500 cycles, but cracks within the grain were observed.

In addition to ceria, McDaniel et al. have investigated three different combinations of La-Sr-Mn-Al perovskites and used LSMA4664 to demonstrate 80 redox cycles in a stagnation flow reactor combined with a laser and resistive heating [15]. The samples were cycled between 1350 °C in He and 850 °C in 40 vol% CO_2 for 15 min, and retained its single-phase structure as well as a constant level of CO production. More recently, Carrillo et al. have investigated Cr incorporated $La_{0.6}Sr_{0.4}MnO_3$ perovskites,

namely LSCM10 through LSCM85 with the two digit number after LSCM indicating the percentage of Cr concentration, and cycled the LSCM85 15 times in a furnace-based alumina reactor [20].

Because the prior studies that cycled under direct radiative heating were at large kW reactor scales where the bulk plays a large role in the overall observed performance, this study aimed to perform temperature-swing thermochemical cycling using a directly irradiated sample at a smaller scale (~200 W) than is typical. The motivation for this is derived from the fact that, at small scales, a higher percentage of the reacting area is near the irradiated surface compared to larger scales, which should elucidate degradation mechanisms more rapidly than in larger systems.

2. Experimental Methods

A schematic of the laser based heating system is shown in Figure 1. A 200 W CO_2 laser (Lightwave KT200, 10.6 µm, 200 W, Kern Technologies) is utilized as a heating source. The laser beam is approximated as a Gaussian beam with a diameter of 11 mm. An aperture machined from porous alumina fiberboard (Buster M-35, Zircar Zirconia, Inc., Orange County, NY, USA) is placed at the beam exit of the laser to physically limit the laser beam diameter to 10 mm. An annular pipe that isolates the delivered gas from the surroundings is connected to a 6-way ConFlat (CF) stainless steel cube sample chamber and is enclosed by a ZnSe window. More details of the laser-based heating system are described in a previous work [21].

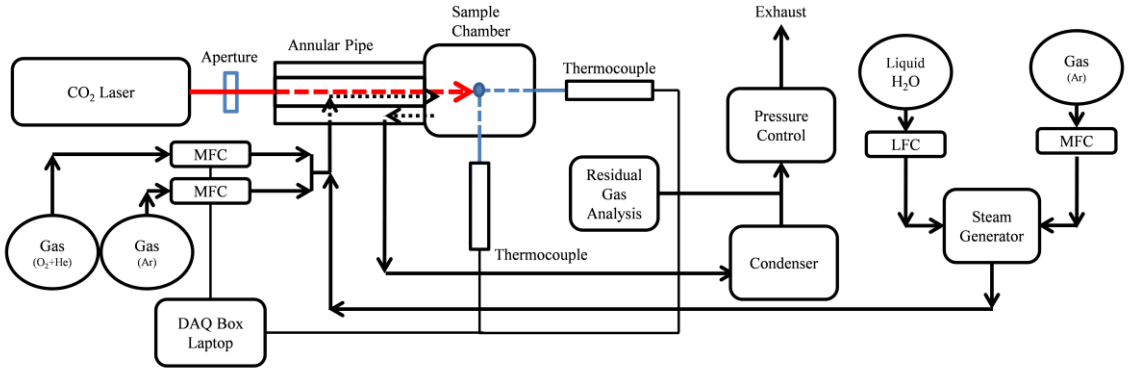


Figure 1. A schematic of a laser-based heating system coupled with a mass spectrometry.

Porous ceria (Alfa Aesar, 5 µm, 99.9%) and LSM40 pellets (synthesized with a modified pechini method described prior [22,23]) were produced by mixing the oxide powders and graphite powder (Alfa Aesar, 2–15 µm, 99.9995%) with a volume ratio of 4:6. A 500 mg mixture of ceria or LSM40 and graphite powders was pelletized with a pellet press (Model 4350 Bench Top press, 12 tons, Carver Inc., El Cajon, CA, USA) and a 13 mm die under 2.5 tons of pressure for 90 s. The graphite was burned during sintering of the pellet at 1550 °C for 5 h in air in a box furnace (RHF 16/8 Box Furnace, 1600 °C, Carbolite, Sheffield, UK). After sintering, the porous ceria pellet had a diameter of 11.27 mm, a thickness of 0.9 mm and 410 mg mass and the LSM40 pellet had a diameter of 11.98 mm, a thickness of 1.22 mm and 404 mg mass.

A sample holder was custom machined from two alumina fiberboards placed back to back (Buster M-35, Zircar Zirconia, Inc.). The front fiberboard has an aperture of 9 mm and on the back side an opening to insert the sample. The second fiberboard is placed on the back to provide insulation. Two type-R thermocouples are placed through 3 mm diameter holes from the back center and from the side of the pellet to monitor temperature.

Experiments were performed one of two ways: either using a constant pO_2 during reduction and oxidation or constant pO_2 for reduction and constant pH_2O for oxidation; in both cases the temperature is changed to induce reduction or oxidation. Constant pO_2 was used for longer-term cycling experiments because of shorter cycle times. For constant pO_2 experiments, two mass flow controllers (GE50A, 500/200 SCCM, MKS Instruments, Andover, MA, USA) deliver 0.1% O_2 balanced

with He and Ar (99.999% purity), respectively, at a total flow rate of 220 SCCM. In the case of H_2O splitting, a liquid flow controller (Liqui-Flow L13V12, 9 g/hr H_2O, Bronkhorst Inc., Bethlehem, PA, USA) delivers 0.2 g/hr liquid H_2O and a mass flow controller (GE50A, 200 SCCM, MKS Instruments) delivers 300 SCCM of Ar to the evaporator (CEM Evaporator W102A-220K, Bronkhorst Inc.). The evaporator is set at 200 °C to vaporize the H_2O, and the H_2O/Ar mixture is delivered to the inlet of the annular pipe where it is mixed with 60 SCCM Ar and delivered to the sample downstream. During reduction, the liquid flow is set to zero. The gases are exhausted through an outer channel of the annular pipe and are sampled via residual gas analysis (QMS100, Stanford Research Systems, Sunnyvale, CA, USA) at the exit of the annular pipe.

For H_2O splitting, reduction was performed by maintaining 19% and 18% duty cycles of the laser power for ceria and LSM40, respectively, for 13.3 min. Similarly, oxidation was performed by switching to 9% duty cycle of the laser power for 13.3 min for ceria. For LSM40, oxidation was performed at 5–7% duty cycles of the laser power for 20 min except for the fourth cycle where oxidation was performed for 40 min. For constant pO_2 experiments, reduction was performed by maintaining 21% duty cycles of the laser power for 6.7 min, and oxidation was performed by switching to 9% duty cycles of the laser power for 13.3 min, where each oxidation reaction was allowed to proceed to equilibrium. The reduction and oxidation extents were determined via integrating consumption or production curves of O_2 or H_2 as it deviated from the baseline. Quantification of consumption or production was determined following a 5-point calibration performed daily. During extended cycling, 10–20 cycles were performed per day and the pellet was cooled to room temperature afterwards. The reaction rate during reduction and oxidation were calculated by averaging the rate during the entire reduction period and the rate until 90% of the initial oxidation state was reached, respectively.

The CO_2 laser, which is the sole heat source of the system, can be approximated as a Gaussian beam and thus has a high flux gradient in the radial direction. The average heat flux over the entire laser spot during reduction at 21% laser power was 1100 kW/m^2, which was calculated by measuring the laser power and the irradiated spot size. The peak heat flux at the center of the laser beam during reduction was 2300 kW/m^2, calculated based on the Gaussian beam assumption, which is shown as follows:

$$I_p = \frac{2P}{\pi w^2}, \quad (1)$$

I_P is the peak intensity, P is the laser power, and w is the Gaussian beam radius. In addition, the heat transfer across the radial direction from the center to the edge of the pellet is limited due to low thermal conductivity of ceria (k = 5.47 W/mK at 973 K) [24]. The thermal conductivity becomes even lower with the porous structure, and the effective thermal conductivity of ceria depends on the porosity [25]. Therefore, the temperature difference between the back center (T_{BC}) and the side (T_S) of the pellet is often as high as 300 °C.

X-ray powder diffraction (XRD) was performed for the LSM40 powder at 2θ CuKα configuration from 20° to 80°. Inductively coupled plasma mass spectrometry (ICP-MS) was performed for the LSM40 powder with aqua regia (HNO_3 + 3HCl) as a dissolving solvent to determine the elemental composition.

A scanning electron microscope (SEM) image of the porous ceria pellet before cycling was taken at 1000× magnification, 3 kV accelerating voltage and 6.0 to 7.0 mm working distance with the secondary electron detection mode. SEM images of the porous ceria pellet after 10 and 200 cycles were taken near the edge (4–6 mm from the center), between the edge and the center (2–4 mm from the center), and near the center (0–2 mm from the center) of the pellet's front surface with the same SEM parameters to that before cycling. Low magnification images were taken at 250×.

Energy dispersive X-ray spectroscopy (EDX) was performed to determine the distribution of elements on the pellet surface. The accelerating voltage was at 15 kV, working distance was at 6.1 mm, and the spot size was 4. A corresponding SEM image of the LSM40 pellet was taken at 3000×.

Mercury intrusion porosimetry (MIP) was performed to investigate the changes in pore volume, specific surface area and porosity of the pellets after 10 and 200 cycles relative to those before cycling.

Hg contact angles for intrusion and extrusion were 140°. At high-pressure setup, pressure ranges were 20–59,685 psia and corresponding pore diameter ranges were 10.653–0.004 µm. At low-pressure setup, pressure ranges were 0.74–50 psia and corresponding pore diameter ranges were 288–4.26 µm.

3. Results and Discussion

3.1. Characterization of Porous Ceria and Porous LSM40

The XRD pattern of fresh LSM40 powder is shown in Figure 2 and alongside comparisons to the literature [16,26,27] are shown in Figure S1. XRD confirmed the perovskite structure of LSM40 powder with rhombohedral distortions in space group $R\bar{3}c$ [26,27]. ICP-MS analysis indicated that the bulk composition of the LSM40 powder is 50.8%, 20.53% and 28.67% for Mn, Sr and La, respectively. The atomic fraction of Sr and La are 0.417 and 0.583, respectively, which is less than 5% error relative to the desired composition.

Shown in Figure 3 are SEM micrographs of the synthesized porous ceria and porous LSM40 pellets, alongside EDX maps of the LSM40 pellet. As seen in the EDX maps, the distribution of La, Sr, Mn, and O indicate that each element is uniformly distributed on the surface except where the pores are located. EDX maps for 3 additional areas on the surface are shown in Figure S2. The target porosity prior to synthesis was 0.4, and the measured bulk porosity based on mass and volume measurements for ceria and LSM40 are 0.3467 and 0.5207, respectively.

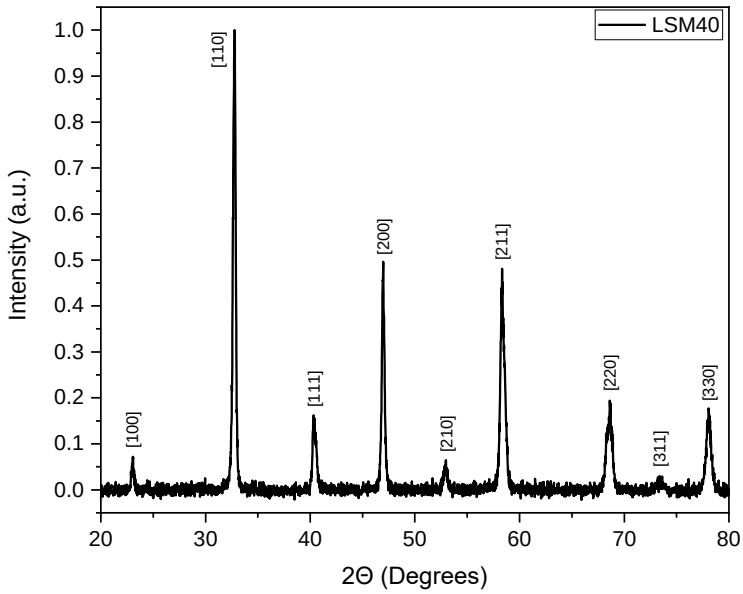


Figure 2. X-ray diffraction (XRD) patterns of the fresh LSM40 powder.

3.2. H_2O Splitting Temperature-Swing Cycling Using Porous Ceria and LSM40

Prior to long-term cycling, which is conducted at a constant pO_2, we aimed to validate the reduction and oxidation power inputs that are used by ensuring H_2O splitting is viable under these conditions. H_2O splitting during consecutive temperature-swing cycles is shown in Figure 4 using a porous ceria pellet. The sample was initially heated to 1300 °C in Ar, which initiated the first reduction of ceria. The pellet was then cycled between 19% and 9% duty cycles of the laser power that corresponded to back surface temperatures between 1300 °C and 900 °C, respectively. pH_2O was kept low at 1.3×10^{-2} atm to prevent condensation on the tubing and the estimated pO_2 was of 3.5×10^{-14} atm. H_2 production during the first cycle can be seen on the far left side of Figure 4, which was initiated by introducing H_2O and decreasing the laser power from 19% to 9%. Total H_2 production was 202 µmol/g for the first cycle and then decreased to 140, 126, 130 and 138 µmol/g for cycles 2, 3, 4 and 5, respectively. This corresponds to a change in non-stoichiometry ($\Delta\delta$) of 0.0348 for

the first cycle and 0.0241, 0.0217, 0.0224, and 0.0237 for cycles 2, 3, 4 and 5, respectively. The decrease in H_2 production after the first cycle is likely due to a limitation of the reaction time because of a decrease in reaction rate: note that the peak rates decreased over the first two cycles.

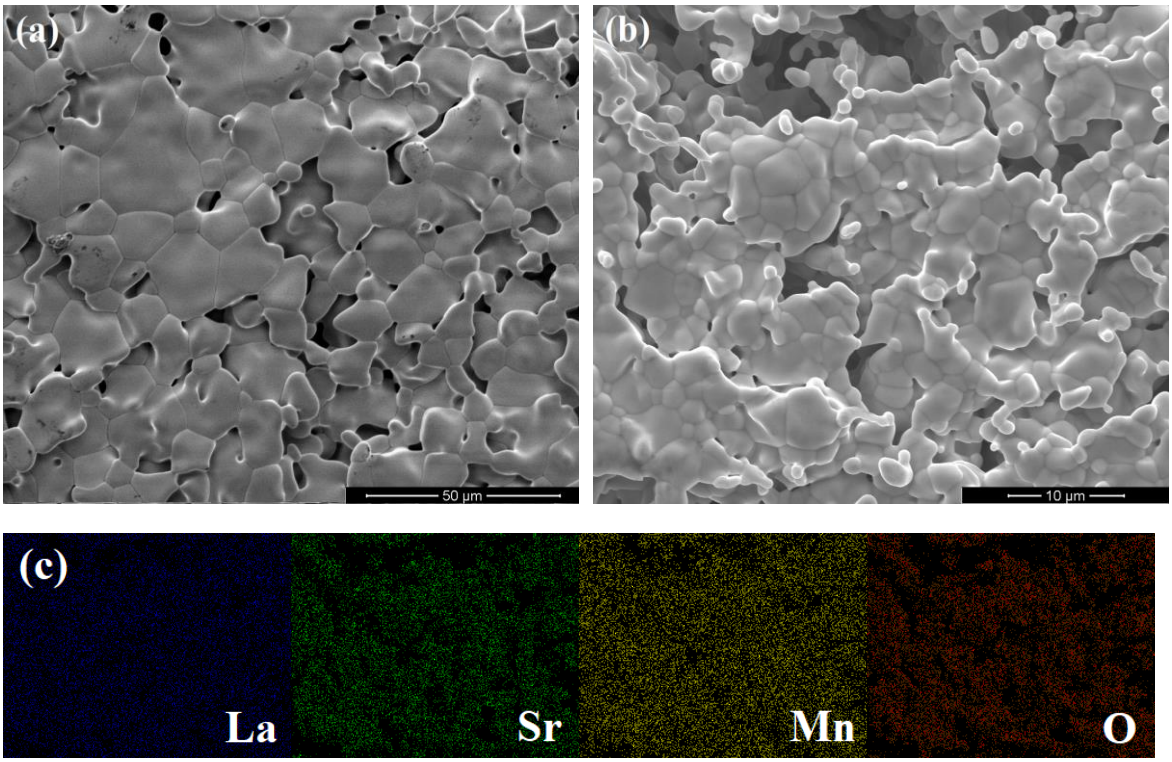


Figure 3. Scanning electron microscopy (SEM) images of: (**a**) The porous ceria pellet, (**b**) The porous LSM40 pellet before cycling and (**c**) the corresponding energy dispersive X-ray spectroscopy (EDX) maps of the porous LSM40 pellet.

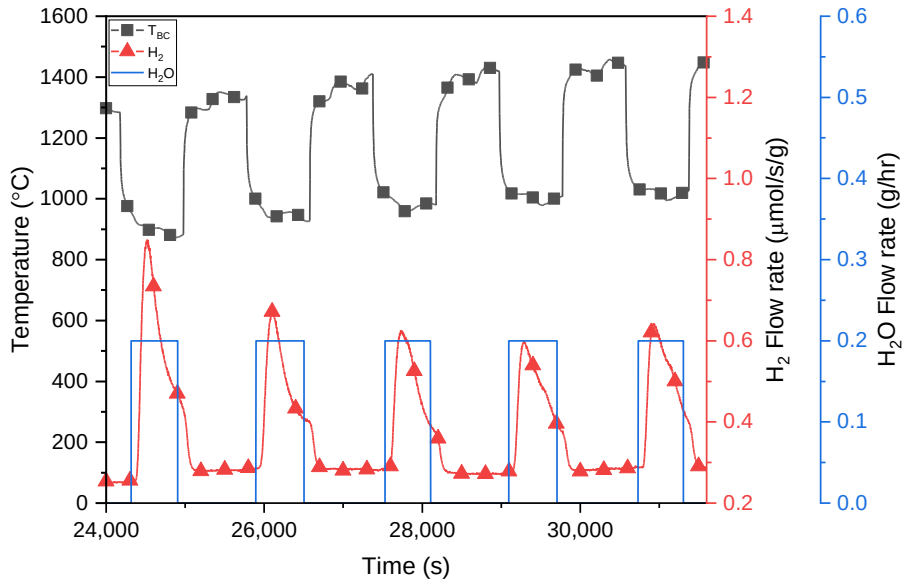


Figure 4. H_2 and H_2O rates vs. time during 5 consecutive temperature-swing cycles with H_2O splitting and the corresponding temperature profile of porous ceria. Symbols are for visual purposes only; the fidelity of measurements was on the order of 2 s.

H_2O splitting during consecutive temperature-swing cycles using a porous LSM40 pellet is shown in Figure 5 with H_2O input, H_2 output and corresponding T_{BC}. First, reduction was induced by heating from room temperature to 1300 °C by increasing the laser power to 19% duty cycle. Oxidation for LSM40 was performed at 7% and 5% duty cycles of the laser power to investigate the changes in H_2 production of LSM40 with changes in oxidation conditions, with the corresponding temperatures between 700 and 500 °C, respectively. Total H_2 production for cycles 1, 2, 3, and 4 were 8 (700 °C), 27 (500 °C), 17 (700 °C), and 55 (500 °C) µmol/g, respectively. This corresponds to the $\Delta\delta$ of 0.0019, 0.0059, 0.0038, and 0.0121 for cycles 1, 2, 3, and 4, respectively. The H_2 rates were higher when the oxidation temperature was lower, presumably because oxidation is thermodynamically more favorable at very low temperatures compared to ceria [28]. The H_2 production was greater for cycle 4 because oxidation was performed for twice as long as cycle 1–3 to see if equilibrium could be established in a reasonable time. However, the reaction was not equilibrated even after 40 min and was much slower than ceria because of the kinetic limitations at low temperature. Figure 6 shows a side by side comparison of H_2 production versus time of porous ceria and LSM40 pellets, respectively. Overall, it is clear that H_2 production of ceria during oxidation was much higher than that of LSM40, regardless of oxidation temperature. It should be noted however that this trend is at least partly due to the low pO_2 during oxidation (like ceria, pH_2O was kept low at 1.3×10^{-2} atm to prevent condensation), where the oxidation is much less favorable for LSM40 than that for ceria [28–30]. Calculated pO_2 during oxidation at 700 °C and 500 °C are 3.5×10^{-14} atm and 2.3×10^{-19} atm, respectively. Thermodynamic calculations based on data from Panlener et al. [29] and Mizusaki et al. [28,30], for reduction at 1300 °C and pO_2 of 5.2×10^{-8} atm, predicted δ_{red} values of 0.0387 and 0.1583 for ceria and LSM40, respectively. However, because of unfavorable oxidation properties of LSM40, the predicted corresponding $\Delta\delta$ values were 0.0346 and 0.0109 for ceria and LSM40, respectively. Although these values do not quantitatively agree with our measurements because of uncertainty in the overall bulk temperature because of surface heating, the overall trends explain the rationale for the much lower LSM40 yields. Thus, we can conclude that, at least for the conditions achievable in our system, ceria is the ideal candidate to investigate for longer-term cycling.

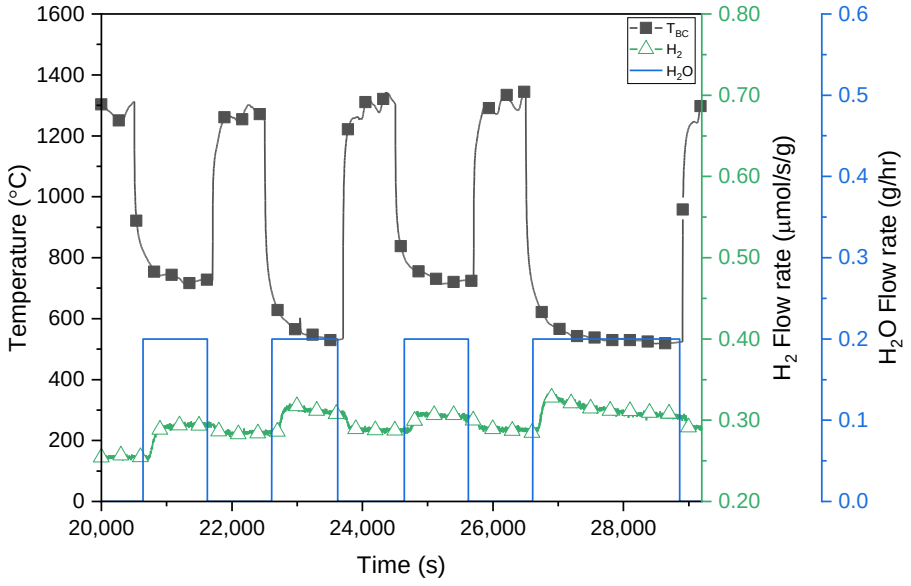


Figure 5. H_2 and H_2O rates vs. time during 4 consecutive temperature-swing cycles with H_2O splitting and the corresponding temperature profile of porous LSM40. Symbols are for visual purposes only.

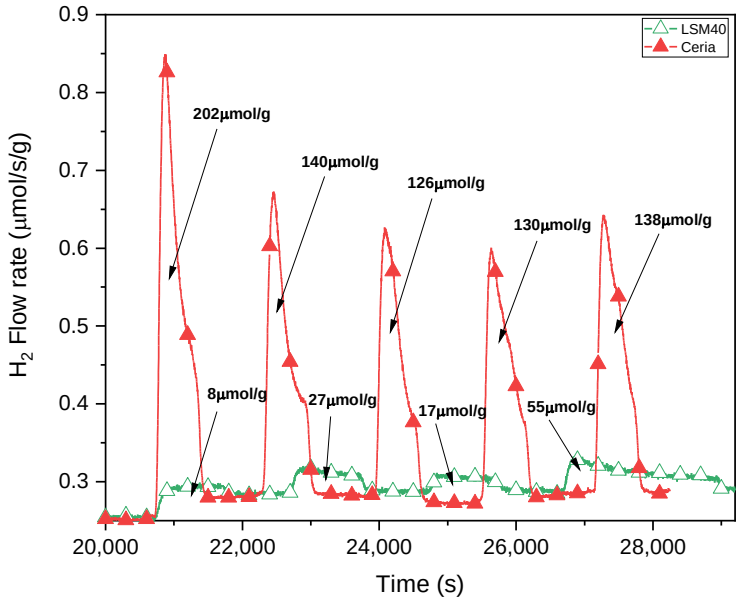


Figure 6. Comparison in H_2 production during 5 and 4 consecutive temperature-swing cycles with H_2O splitting of porous ceria and LSM40 pellets, respectively. Numbers in µmol with arrows are the total H_2 production for each reaction. Symbols are for visual purposes only.

3.3. Temperature-Swing Cycling of Porous Ceria at Constant pO_2

After validating power input for reduction and oxidation, longer-term temperature-swing cycling at constant pO_2 (0.1% O_2 balanced with He and Ar) was performed with a porous ceria pellet over 200 cycles. Although the change in non-stoichiometry for a constant pO_2 will be different than cycling between different pO_2's (Ar, then H_2O), we expect that the major degradation mechanisms are due to sintering [6], sublimation [31,32] or phase changes [33], rather than thermal [34] or chemical [35] expansion, which have comparable magnitudes under the considered reaction conditions. O_2 production and consumption during two exemplary temperature-swing cycles with corresponding temperature profiles are shown in Figure 7a. Reduction and oxidation were initiated only by the change in laser power between 21% and 9% duty cycle, and the corresponding temperatures were 1300 °C and 850 °C, respectively. Therefore, reduction and oxidation could be characterized by either production or consumption of oxygen, and a deviation from the baseline established by the trace O_2 introduced to the system. The ideal O_2 baseline is shown as a flat dashed line. O_2 production during reduction was 42.56 and 41.95 µmol/g, respectively, and corresponding δ_{red} were 0.0073 and 0.0072, respectively. The small peak in O_2 at the end of each reduction is due to the increase in temperature, which is related to the periodic temperature fluctuation attributed to the unsmoothed waveform of the power supply driving the laser discharge tubes [36]. The O_2 consumption during oxidation was 38.98 and 36.08 µmol/g, respectively, and corresponding $\Delta\delta$ were 0.0067 and 0.0062, respectively. The O_2 consumption rate during oxidation remained constant for 600 s before it increased back to baseline. This behavior is likely a result of a limited mass flow rate of O_2. On the other hand, reduction of ceria is likely limited by the rate of heat transfer from the front surface of the pellet to the back [1,37]. O_2 production and consumption during the first 10 consecutive temperature-swing cycles with corresponding temperature profiles of a porous ceria pellet are shown in Figure 7b. The first reduction was initiated by the step-wise increase in laser power during heating, which is shown as multiple small peaks of O_2 instead of one large peak that is typical. The O_2 production ($O_{2,red}$) and consumption ($O_{2,ox}$) during the first 10 temperature-swing cycles and corresponding δ_{red}, $\Delta\delta$, O_2 rate during reduction and oxidation are tabulated in Table 1. The average $O_{2,red}$ and $O_{2,ox}$ were 42.55 and 38.29 µmol/g, respectively, with a corresponding average δ_{red} and $\Delta\delta$ of 0.0073 and 0.0067, respectively. Overall, total $O_{2,red}$ during reduction and total $O_{2,ox}$ during oxidation decreased from cycle 1 to cycle

10 by 10% and 8%, respectively. The decrease in O_2 production is due to the decrease in O_2 rate during reduction.

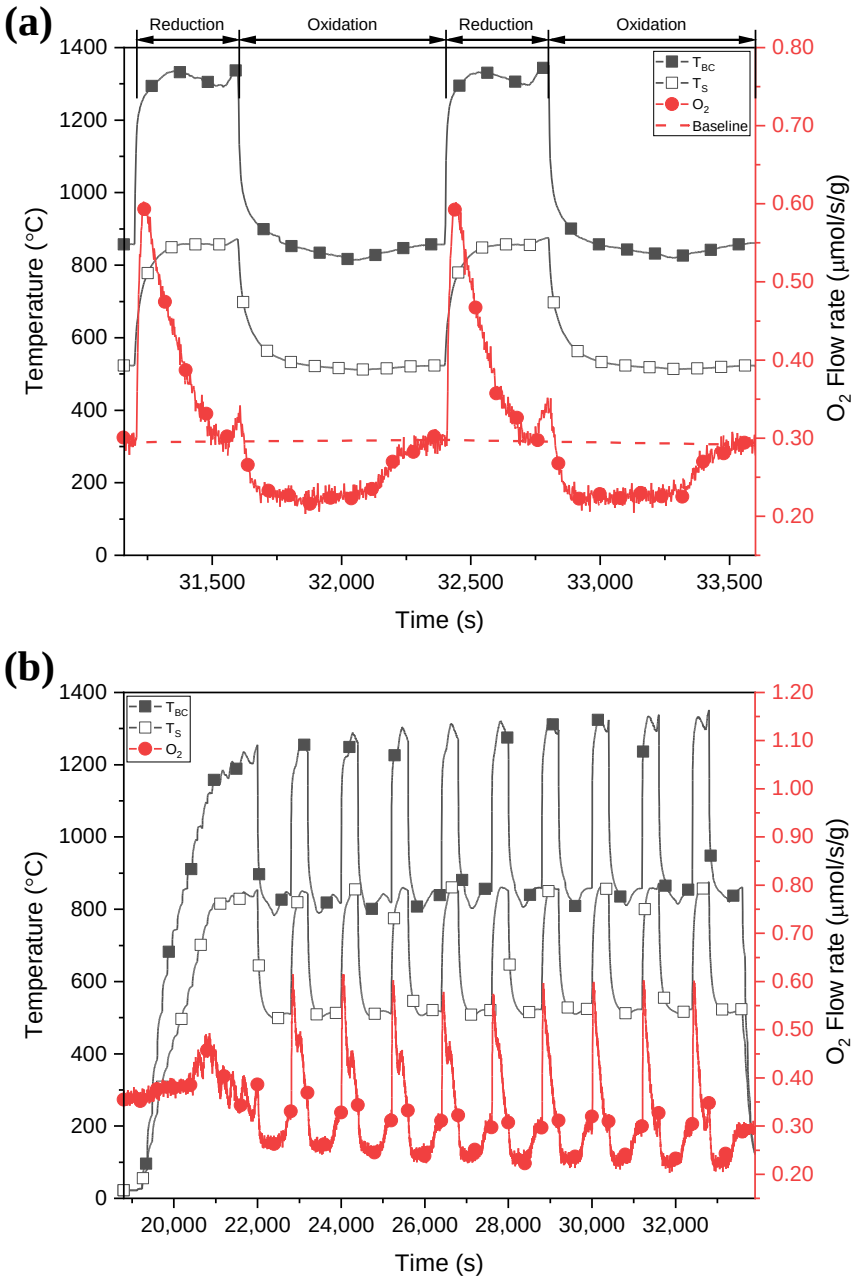


Figure 7. O_2 production and consumption during (**a**) exemplary temperature-swing cycles and (**b**) first 10 temperature-swing cycles with constant pO_2, and corresponding temperature profiles of porous ceria. Symbols are for visual purposes only.

Table 1. O_2 production and consumption during the first cycles and corresponding reduction extents, changes in non-stoichiometry, O_2 rate during reduction and oxidation.

N_{cycle}	$O_{2,red}$ (μmol/g)	$O_{2,ox}$ (μmol/g)	δ_{red}	$\Delta\delta$	$Rate_{red}$ (μmol/s/g)	$Rate_{ox}$ (μmol/s/g)
1	45.67	38.67	0.0079	0.0067	0.0399	0.0579
2	44.50	36.54	0.0077	0.0063	0.1113	0.0617
3	43.77	40.42	0.0075	0.0070	0.1068	0.0651
4	45.19	40.26	0.0078	0.0069	0.1119	0.0637
5	42.02	40.24	0.0072	0.0069	0.1046	0.0671
6	41.54	37.49	0.0072	0.0065	0.1039	0.0633
7	41.80	37.64	0.0072	0.0065	0.1056	0.0637
8	40.23	40.10	0.0069	0.0069	0.0987	0.0669
9	39.72	36.01	0.0068	0.0062	0.0960	0.0616
10	41.09	35.54	0.0071	0.0061	0.0974	0.0626

δ_{red} and the $\Delta\delta$ for the total of 200 temperature-swing cycles are shown in Figure 8. δ_{red} initially was 0.0075 for the first 5 cycles, but decreased to 0.0064 during the cycles 30 to 35. The decrease in the δ_{red} continued almost linearly with cycling number, but became flatter near cycle 120 for the remainder of cycles. The average δ_{red} between cycle 120 and 200 was 0.0044 ± 0.0004. $\Delta\delta$ decreased from 0.0067 (first 5 cycles) to 0.0060 for cycles 30 to 35 and the average $\Delta\delta$ between cycle 120 and 200 was 0.0041 ± 0.0004.

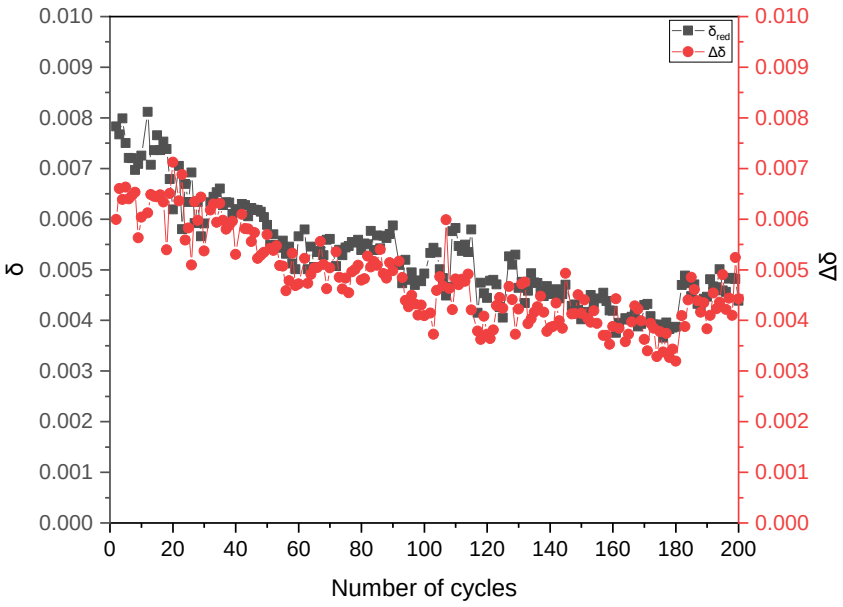


Figure 8. Change in non-stoichiometry and reduction extent during the course of 200 temperature-swing cycles.

The mean O_2 rate during reduction and oxidation versus cycle number are shown in Figure 9. The O_2 rate during reduction followed a very similar trend to the δ_{red}, where it decreased nearly linearly over the first 120 cycles and stabilized for longer times. The initial mean O_2 rate during reduction from cycles 1–5 was 0.1077 μmol/s/g and decreased to 0.0638μmol/s/g, almost 60% of the initial value, at cycle 121–125. Between cycle 120 and 200 the mean O_2 rate was 0.0633 ± 0.0051 μmol/s/g. Unlike O_2 rate during reduction, O_2 rate during oxidation overall was consistent at an average of 0.0642 ± 0.0050 μmol/s/g over 200 cycles. (0.0642 μmol/s/g for cycles 1–5, 0.0602 μmol/s/g for cycles 121–125, and 0.0618 μmol/s/g for cycles 120–200) Again, this is a result of the fact that the reaction rate is limited by the O_2 delivery rate. Because the O_2 rate during reduction decreased and the time was fixed, these slower rates, rather than thermodynamic limitations due to phase transformations, likely caused the decrease in total δ_{red}. Because the rate during reduction is mainly limited by the heat

transfer rate through the sample because of very rapid oxygen diffusion rates [5,38,39], we expect that decrease in the mean O_2 rate during reduction is likely related to structural changes (e.g, sintering and densification) that decrease the effective conductivity, decreasing heat transfer rates from the surface to the back and sides of the pellet.

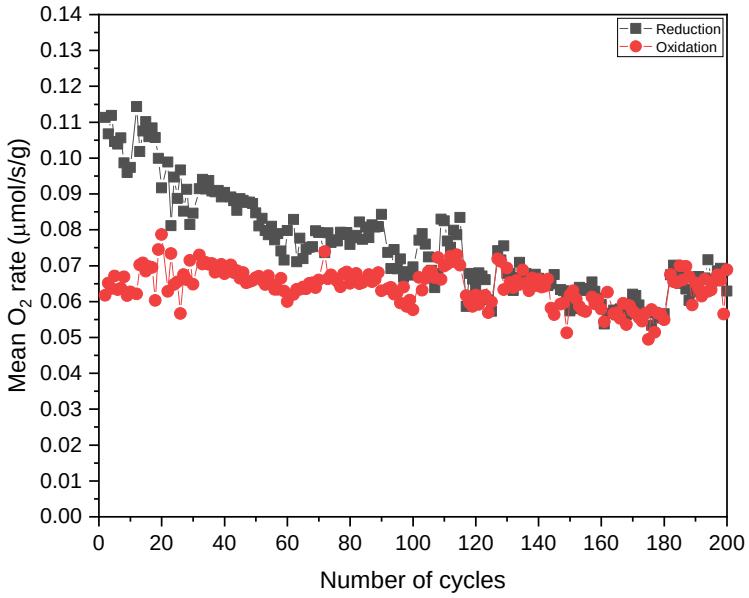


Figure 9. Mean reaction rates during reduction and oxidation per gram of ceria during the course of 200 temperature-swing cycles.

SEM images of the cycled porous ceria after 10 cycles and after 200 cycles were obtained to investigate the surface morphology after thermal cycling. SEM images of the porous ceria pellet after 10 cycles near the edge, between the edge and the center, and near the center are shown in Figure 10. Near the edge of the pellet, the porous structure was retained with clearly-visible grain boundaries: the average grain size near the edge of the pellet was 13.84 μm. Between the edge and the center, there was some noticeable degradation of the porous structure due to sintering; here average grain size was 23.20 μm. Near the center where the highest temperatures were expected, growth of columnar pyramid structures was observed (Figure 10d) at low magnification. Some of the porous structure between the columns were visible, but pores were not observed in the columns at all. There was a high degree of sintering and here it was difficult to identify the grain boundaries at all.

SEM images of the porous ceria pellet after 200 cycles near the edge, between the edge and the center, and near the center are shown in Figure 11. Near the edge, the porous structure was still preserved even after 200 cycles, but the average grain size increased to 20.10 μm. Between the edge and the center, more sintering and grain growth was observed, but the grain boundaries were still apparent; the average grain size increased slightly to 25.75 μm. The growth of columnar pyramid structure near the center progressed even further after 200 cycles.

The growth of the columnar structure has been reported for ceria [40] and doped-ceria [41,42] thin films with crystalline microstructure, as well as ceria fiber [43]. A combination of columnar and dendritic growth of a ceria thin film was reported at T = 473–773 K, and pyramidal formations of columns were observed at T = 773 K in the scale of hundreds of nanometers [40]. However, the growth of the columnar pyramid structure in larger scales (i.e., hundreds of micrometers) is not well documented. The high laser heat flux (2300 kW/m^2 at the center at 21% duty cycle of the laser power) concentrated at the center of the pellet could in theory heat the center to well beyond the 1300 °C measured at the back surface of the pellet. For example, we estimated that under stagnation conditions and assuming blackbody properties, the temperature could be as high as 2250 °C, which is close to the melting point of ceria at 1950–2400 °C [44]. Considering that the growth of the columnar

pyramid structure was already present after 10 cycles, the decrease in the O_2 rate during reduction for the first 30 cycles is possibly due to these structural changes.

MIP was performed for the porous ceria pellet before cycling, after 10 cycles and 200 cycles to investigate the degrees of sintering with possible changes in specific surface area and effective porosity (excluding the isolated pores). The intrusion and extrusion curves indicating normalized volume versus pore size are shown in Figures S3–S5 for the porous ceria pellet before cycling, after 10 cycles and 200 cycles, respectively. The pore volume distribution indicated that small pores with pore diameter below 10^{-2} µm decreased in volume as cycles progressed. Total pore volumes, specific surface area (SSA) and effective porosity from the MIP data at high-pressure and low-pressure configurations are summarized in Tables 2 and 3, respectively. Overall, the total pore volumes, specific surface area and effective porosity decreased as number of cycles progressed, which are most likely due to sintering. Based on the decrease of pore volumes and porosity, the degree of sintering is more significant during the initial 10 cycles compared to the latter 190 cycles, which is similar in trend with the structural change observed from the SEM results.

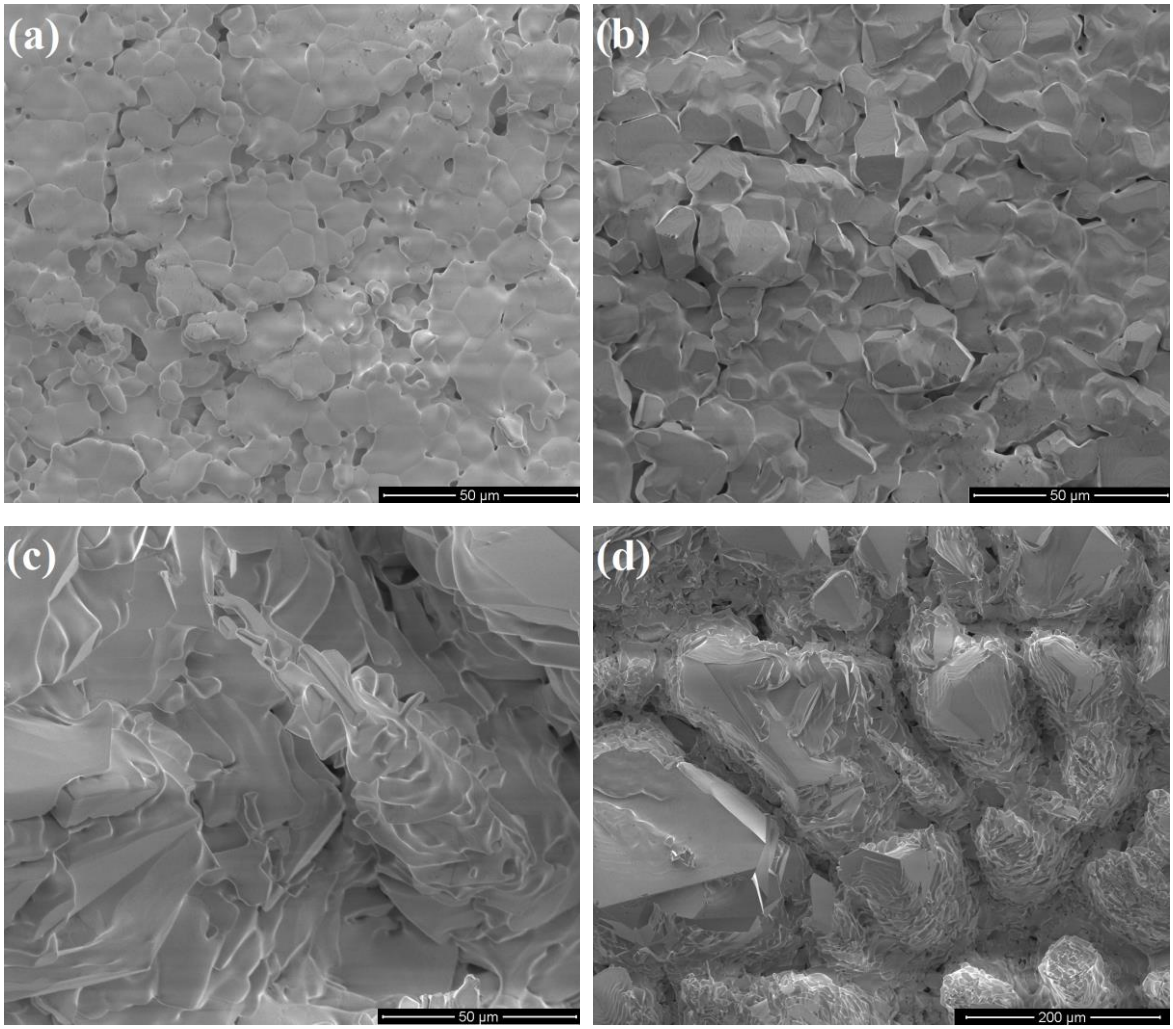


Figure 10. SEM images of the porous ceria pellet after 10 cycles: (**a**) near the edge; (**b**) between the edge and the center; (**c**) near the center; (**d**) near the center with low magnification. All images are at 1000× magnification except (**d**), which is at 250× magnification.

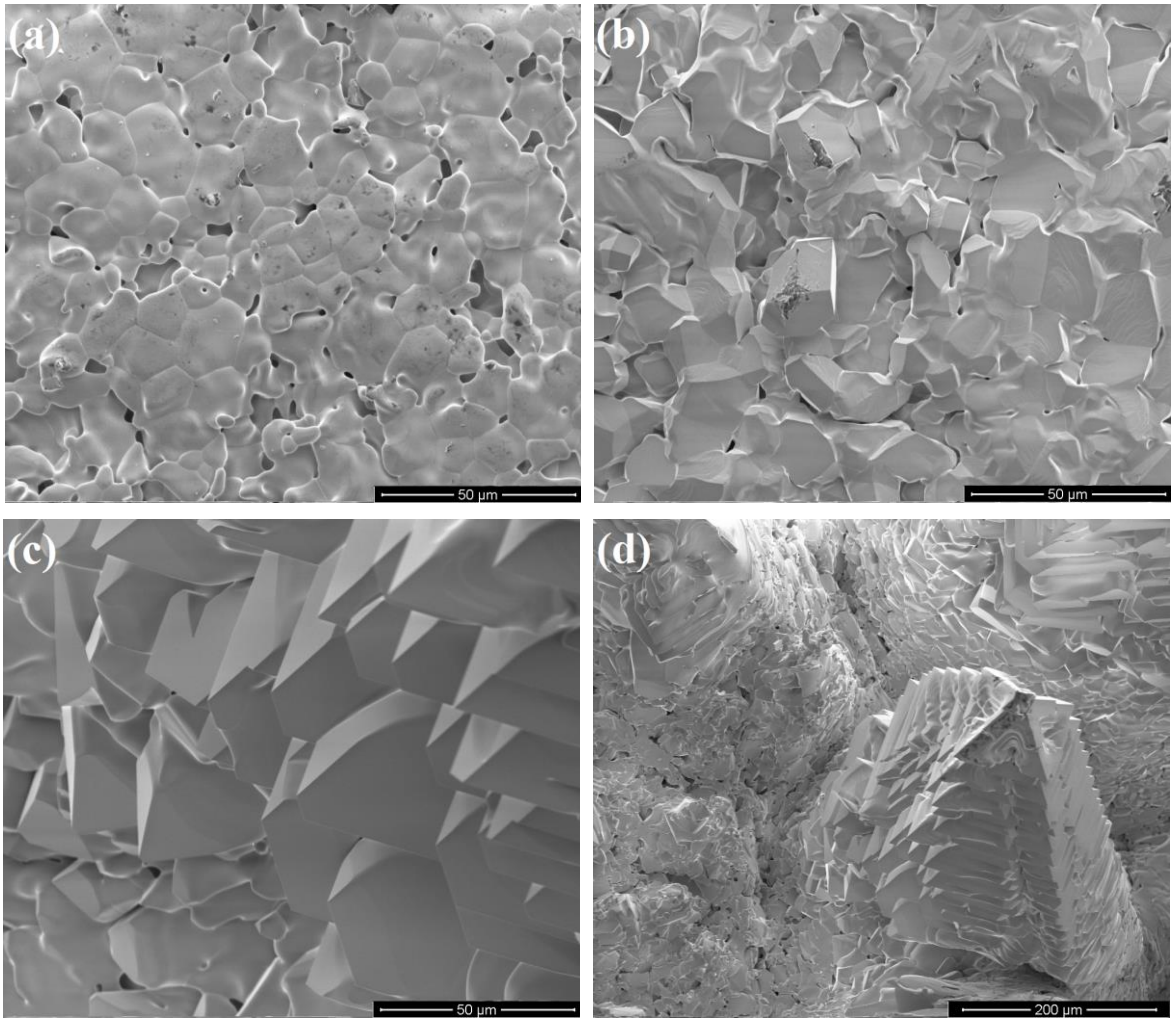


Figure 11. SEM images of the porous ceria pellet after 200 cycles: (**a**) near the edge; (**b**) between the edge and the center; (**c**) near the center; (**d**) near the center with low magnification. All images are at 1000× magnification except (**d**), which is at 250× magnification.

Table 2. Total pore volumes, specific surface area (SSA) and effective porosity of ceria before cycling, after 10 cycles and after 200 cycles from mercury intrusion porosimetry (MIP) analysis at high-pressure configuration.

Material	Pore Volumes (cc/g)	SSA (m^2/g)	Effective Porosity
Ceria (before cycling)	0.0764	18.6778	0.5509
Ceria (after 10 cycles)	0.0625	4.2121	0.4519
Ceria (after 200 cycles)	0.0518	0.0507	0.3742

Table 3. Total pore volumes, specific surface area and effective porosity of ceria before cycling, after 10 cycles and after 200 cycles from MIP analysis at low pressure configuration.

Material	Pore Volumes (cc/g)	SSA (m^2/g)	Effective Porosity
Ceria (before cycling)	0.1226	0.0508	0.8838
Ceria (after 10 cycles)	0.0796	0.0355	0.5752
Ceria (after 200 cycles)	0.0778	0.0264	0.5615

4. Conclusions

In this work, we demonstrated thermochemical redox cycles driven by direct irradiation of porous samples at a much smaller scale than is typical of solar reactors. H_2O splitting of porous ceria and LSM40 pellets via temperature-swing cycling were demonstrated and H_2 production was stable for the porous ceria pellet at an average of 133.53 ± 6.57 μmol/g after the first cycle. H_2 production for the porous LSM40 pellet was significantly lower compared to that of ceria because of the low pO_2 during oxidation, where the oxidation is less favorable for LSM40 than that for ceria.

Longer-term cycling at constant pO_2 for the porous ceria pellet was investigated via 200 temperature-swing cycles. Reaction rates and extents decreased during the first 120 cycles but stabilized afterwards. This was likely caused by a decrease in the effective thermal conductivity, resulting in decreased heat transfer rates through the sample, as evidenced by sintering observed in SEM micrographs. These showed that at the center where the radiative flux and temperature are highest, the growth of columnar pyramid structure was observed in place of the porous structure. Sintering of the porous ceria pellet during cycling was also quantified via MIP, and the degree of sintering was more significant during an initial 10 cycles compared to the following 190 cycles. This supports the observations that the deactivation occurs relatively quickly during the first 10 to 20 cycles and then slows down.

This work demonstrates that the extreme radiative heat flux expected on the surface of redox materials in a directly irradiated reactor can be simulated with the laser-based heating system at a smaller scale. It provides fast redox cycling capability and more rapid elucidation of degradation mechanisms compared to larger scale systems because more of the sample surface is heated directly from the high flux source. To extend this work to other material systems and morphologies, we aim to investigate the effect that pore size, distribution and porosity have on the overall stability and hope to improve strategies for synthesizing stable reactive structures in reactor-scale systems.

Supplementary Materials: The following are available online at http://www.mdpi.com/1996-1073/13/22/5935/s1, Figure S1: Comparison of the XRD patterns of the fresh LSM40 powder to the literature, Figure S2: EDX images of the porous LSM40 pellet for 5 additional areas on the surface, Figure S3: MIP intrusion and extrusion curves of a porous ceria pellet before cycling with normalized pore volume versus pore diameter, Figure S4: MIP intrusion and extrusion curves of a porous ceria pellet after 10 cycles with normalized pore volume versus pore diameter, Figure S5: MIP intrusion and extrusion curves of a porous ceria pellet after 200 cycles with normalized pore volume versus pore diameter.

Author Contributions: Conceptualization, K.L. and J.R.S.; methodology, K.L. and J.R.S.; validation, J.R.S.; formal analysis, K.L.; investigation, K.L. and J.R.S.; resources, J.R.S.; data curation, K.L.; writing—original draft preparation, K.L.; writing—review and editing, J.R.S.; visualization, K.L.; supervision, J.R.S.; project administration, J.R.S.; funding acquisition, J.R.S. All authors have read and agreed to the published version of the manuscript.

Funding: This research was funded by the College of Engineering and the Department of Mechanical and Aerospace Engineering in the University of Florida.

Acknowledgments: The authors also thank Caitlin Tibbetts and Gary Scheiffele for MIP analysis, Richard Carrillo for helping with the perovskite synthesis and Caroline Hill for helping with the perovskite characterization.

Conflicts of Interest: The authors declare no conflict of interest.

References

1. Chueh, W.C.; Falter, C.; Abbott, M.; Scipio, D.; Furler, P.; Haile, S.M.; Steinfeld, A. High-Flux Solar-Driven Thermochemical Dissociation of CO2 and H2O Using Nonstoichiometric Ceria. *Science* **2010**, *330*, 1797–1801. [CrossRef] [PubMed]
2. Scheffe, J.R.; Steinfeld, A. Oxygen exchange materials for solar thermochemical splitting of H2O and CO2: A review. *Mater. Today* **2014**, *17*, 341–348. [CrossRef]
3. Romero, M.; Steinfeld, A. Concentrating solar thermal power and thermochemical fuels. *Energy Environ. Sci.* **2012**, *5*, 9234–9245. [CrossRef]
4. Smestad, G.P.; Steinfeld, A. Review: Photochemical and Thermochemical Production of Solar Fuels from H2O and CO2 Using Metal Oxide Catalysts. *Ind. Eng. Chem. Res.* **2012**, *51*, 11828–11840. [CrossRef]

5. Chueh, W.C.; Haile, S.M. Ceria as a Thermochemical Reaction Medium for Selectively Generating Syngas or Methane from H2O and CO2. *ChemSusChem* **2009**, *2*, 735–739. [CrossRef]
6. Chueh, W.C.; Haile, S.M. A thermochemical study of ceria: Exploiting an old material for new modes of energy conversion and CO2 mitigation. *Philos. Trans. R. Soc. A Math. Phys. Eng. Sci.* **2010**, *368*, 3269–3294. [CrossRef]
7. Carrillo, R.J.; Scheffe, J.R. Advances and trends in redox materials for solar thermochemical fuel production. *Sol. Energy* **2017**, *156*, 3–20. [CrossRef]
8. Marxer, D.; Furler, P.; Takacs, M.; Steinfeld, A. Solar thermochemical splitting of CO2 into separate streams of CO and O2 with high selectivity, stability, conversion, and efficiency. *Energy Environ. Sci.* **2017**, *10*, 1142–1149. [CrossRef]
9. Scheffe, J.R.; Welte, M.; Steinfeld, A. Thermal Reduction of Ceria within an Aerosol Reactor for H2O and CO2Splitting. *Ind. Eng. Chem. Res.* **2014**, *53*, 2175–2182. [CrossRef]
10. Sørensen, O. Thermodynamic studies of the phase relationships of nonstoichiometric cerium oxides at higher temperatures. *J. Solid State Chem.* **1976**, *18*, 217–233. [CrossRef]
11. Ackermann, S.; Scheffe, J.R.; Steinfeld, A. Diffusion of Oxygen in Ceria at Elevated Temperatures and Its Application to H2O/CO2 Splitting Thermochemical Redox Cycles. *J. Phys. Chem. C* **2014**, *118*, 5216–5225. [CrossRef]
12. Chueh, W.C.; McDaniel, A.H.; Grass, M.E.; Hao, Y.; Jabeen, N.; Liu, Z.; Haile, S.M.; Mccarty, K.F.; Bluhm, H.; El Gabaly, F. Highly Enhanced Concentration and Stability of Reactive Ce3+ on Doped CeO2 Surface Revealed In Operando. *Chem. Mater.* **2012**, *24*, 1876–1882. [CrossRef]
13. Scheffe, J.R.; Weibel, D.; Steinfeld, A. Lanthanum–Strontium–Manganese Perovskites as Redox Materials for Solar Thermochemical Splitting of H2O and CO2. *Energy Fuels* **2013**, *27*, 4250–4257. [CrossRef]
14. Evdou, A.; Zaspalis, V.T.; Nalbandian, L. La(1−x)SrxMnO3−δ perovskites as redox materials for the production of high purity hydrogen. *Int. J. Hydrogen Energy* **2008**, *33*, 5554–5562. [CrossRef]
15. McDaniel, A.H.; Miller, E.C.; Arifin, D.; Ambrosini, A.; Coker, E.N.; O'Hayre, R.; Chueh, W.C.; Tong, J. Sr- and Mn-doped LaAlO3−δ for solar thermochemical H2 and CO production. *Energy Environ. Sci.* **2013**, *6*, 2424–2428. [CrossRef]
16. Takacs, M.; Hoes, M.; Caduff, M.; Cooper, T.; Scheffe, J.R.; Steinfeld, A. Oxygen nonstoichiometry, defect equilibria, and thermodynamic characterization of LaMnO3 perovskites with Ca/Sr A-site and Al B-site doping. *Acta Mater.* **2016**, *103*, 700–710. [CrossRef]
17. Ezbiri, M.; Takacs, M.; Theiler, D.; Michalsky, R.; Steinfeld, A. Tunable thermodynamic activity of LaxSr1−xMnyAl1−yO3−δ ($0 \leq x \leq 1$, $0 \leq y \leq 1$) perovskites for solar thermochemical fuel synthesis. *J. Mater. Chem. A* **2017**, *5*, 4172–4182. [CrossRef] [PubMed]
18. Gladen, A.C.; Davidson, J.H. The morphological stability and fuel production of commercial fibrous ceria particles for solar thermochemical redox cycling. *Sol. Energy* **2016**, *139*, 524–532. [CrossRef]
19. Hathaway, B.J.; Chandran, R.B.; Gladen, A.C.; Chase, T.R.; Davidson, J.H. Demonstration of a Solar Reactor for Carbon Dioxide Splitting via the Isothermal Ceria Redox Cycle and Practical Implications. *Energy Fuels* **2016**, *30*, 6654–6661. [CrossRef]
20. Carrillo, A.J.; Bork, A.H.; Moser, T.; Sediva, E.; Hood, Z.D.; Rupp, J.L.M. Modifying $La_{0.6}Sr_{0.4}MnO_3$ Perovskites with Cr Incorporation for Fast Isothermal CO_2–Splitting Kinetics in Solar–Driven Thermochemical Cycles. *Adv. Energy Mater.* **2019**, *9*, 1803886:1–1803886:13. [CrossRef]
21. Lee, K.; Scheffe, J.R. Characterization of a Laser-Based Heating System Coupled With In Operando Raman Spectroscopy for Studying Solar Thermochemical Redox Cycles. *J. Sol. Energy Eng.* **2019**, *141*, 021013:1–021013:7. [CrossRef]
22. Pechini, M.P. Method of Preparing Lead and Alkaline Earth Titanates and Niobates and Coating Method Using the Same to form a Capacitor. U.S. Patent 3,330,697, 11 July 1967.
23. Cooper, T.; Scheffe, J.R.; Galvez, M.E.; Jacot, R.; Patzke, G.R.; Steinfeld, A. Lanthanum Manganite Perovskites with Ca/Sr A-site and Al B-site Doping as Effective Oxygen Exchange Materials for Solar Thermochemical Fuel Production. *Energy Technol.* **2015**, *3*, 1130–1142. [CrossRef]
24. Khafizov, M.; Park, I.-W.; Chernatynskiy, A.; He, L.-F.; Lin, J.; Moore, J.J.; Swank, D.; Lillo, T.; Phillpot, S.R.; El-Azab, A.; et al. Thermal Conductivity in Nanocrystalline Ceria Thin Films. *J. Am. Ceram. Soc.* **2013**, *97*, 562–569. [CrossRef]

25. Ackermann, S.; Scheffe, J.R.; Duss, J.; Steinfeld, A. Morphological Characterization and Effective Thermal Conductivity of Dual-Scale Reticulated Porous Structures. *Materials* **2014**, *7*, 7173–7195. [CrossRef]
26. Yang, C.-K.; Yamazaki, Y.; Aydin, A.; Haile, S.M. Thermodynamic and kinetic assessments of strontium-doped lanthanum manganite perovskites for two-step thermochemical water splitting. *J. Mater. Chem. A* **2014**, *2*, 13612–13623. [CrossRef]
27. Gálvez, M.E.; Jacot, R.; Scheffe, J.R.; Cooper, T.; Patzke, G.R.; Steinfeld, A. Physico-chemical changes in Ca, Sr and Al-doped La–Mn–O perovskites upon thermochemical splitting of CO2via redox cycling. *Phys. Chem. Chem. Phys.* **2015**, *17*, 6629–6634. [CrossRef] [PubMed]
28. Mizusaki, J.; Tagawa, H. Nonstoichiometry and thermochemical stability of the perovskite-type La1−xSrxMnO3−δ. *Solid State Ion.* **1991**, *49*, 111–118. [CrossRef]
29. Panlener, R.; Blumenthal, R.; Garnier, J. A thermodynamic study of nonstoichiometric cerium dioxide. *J. Phys. Chem. Solids* **1975**, *36*, 1213–1222. [CrossRef]
30. Mizusaki, J. Oxygen nonstoichiometry and defect equilibrium in the perovskite-type oxides La1−xSrxMnO3+d. *Solid State Ion.* **2000**, *129*, 163–177. [CrossRef]
31. Abanades, S.; Legal, A.; Cordier, A.; Peraudeau, G.; Flamant, G.; Julbe, A. Investigation of reactive cerium-based oxides for H2 production by thermochemical two-step water-splitting. *J. Mater. Sci.* **2010**, *45*, 4163–4173. [CrossRef]
32. Furler, P.; Scheffe, J.R.; Steinfeld, A. Syngas production by simultaneous splitting of H2O and CO2via ceria redox reactions in a high-temperature solar reactor. *Energy Environ. Sci.* **2012**, *5*, 6098–6103. [CrossRef]
33. Riess, I.; Ricken, M.; No¨lting, J. On the specific heat of nonstoichiometric ceria. *J. Solid State Chem.* **1985**, *57*, 314–322. [CrossRef]
34. Hayashi, H. Thermal expansion of Gd-doped ceria and reduced ceria. *Solid State Ion.* **2000**, *132*, 227–233. [CrossRef]
35. Bishop, S.; Duncan, K.; Wachsman, E. Defect equilibria and chemical expansion in non-stoichiometric undoped and gadolinium-doped cerium oxide. *Electrochim. Acta* **2009**, *54*, 1436–1443. [CrossRef]
36. Lim, G.; Steen, W. Measurement of the temporal and spatial power distribution of a high-power CO2 laser beam. *Opt. Laser Technol.* **1982**, *14*, 149–153. [CrossRef]
37. Furler, P.; Scheffe, J.R.; Marxer, D.; Gorbar, M.; Bonk, A.; Vogt, U.; Steinfeld, A. Thermochemical CO2 splitting via redox cycling of ceria reticulated foam structures with dual-scale porosities. *Phys. Chem. Chem. Phys.* **2014**, *16*, 10503–10511. [CrossRef] [PubMed]
38. Ackermann, S.; Sauvin, L.; Castiglioni, R.; Rupp, J.L.M.; Scheffe, J.R.; Steinfeld, A. Kinetics of CO2 Reduction over Nonstoichiometric Ceria. *J. Phys. Chem. C* **2015**, *119*, 16452–16461. [CrossRef] [PubMed]
39. Furler, P.; Scheffe, J.; Gorbar, M.; Moes, L.; Vogt, U.; Steinfeld, A. Solar Thermochemical CO2 Splitting Utilizing a Reticulated Porous Ceria Redox System. *Energy Fuels* **2012**, *26*, 7051–7059. [CrossRef]
40. Bârcă, E.; Filipescu, M.; Luculescu, C.; Birjega, R.; Ion, V.; Dumitru, M.; Nistor, L.; Stanciu, G.; Abrudeanu, M.; Munteanu, C.; et al. Pyramidal growth of ceria nanostructures by pulsed laser deposition. *Appl. Surf. Sci.* **2016**, *363*, 245–251. [CrossRef]
41. Mansilla, C.; Holgado, J.P.; Espinós, J.P.; González-Elipe, A.; Yubero, F. Microstructure and transport properties of ceria and samaria doped ceria thin films prepared by EBE–IBAD. *Surf. Coat. Technol.* **2007**, *202*, 1256–1261. [CrossRef]
42. Pryds, N.H.; Rodrigo, K.; Linderoth, S.; Schou, J. On the growth of gadolinia-doped ceria by pulsed laser deposition. *Appl. Surf. Sci.* **2009**, *255*, 5232–5235. [CrossRef]
43. Takacs, M.; Ackermann, S.; Bonk, A.; Puttkamer, M.N.-V.; Haueter, P.; Scheffe, J.R.; Vogt, U.F.; Steinfeld, A. Splitting CO2with a ceria-based redox cycle in a solar-driven thermogravimetric analyzer. *AIChE J.* **2016**, *63*, 1263–1271. [CrossRef] [PubMed]
44. Abanades, S.; Flamant, G. Thermochemical hydrogen production from a two-step solar-driven water-splitting cycle based on cerium oxides. *Sol. Energy* **2006**, *80*, 1611–1623. [CrossRef]

Publisher's Note: MDPI stays neutral with regard to jurisdictional claims in published maps and institutional affiliations.

© 2020 by the authors. Licensee MDPI, Basel, Switzerland. This article is an open access article distributed under the terms and conditions of the Creative Commons Attribution (CC BY) license (http://creativecommons.org/licenses/by/4.0/).